ACS Photonics

Article

pubs.acs.org/journal/apchd5

Coherent Four-Fold Super-Resolution Imaging with Composite Photonic–Plasmonic Structured Illumination

Antonio I. Fernández-Domínguez,*[,†,‡] Zhaowei Liu,[§] and John B. Pendry[†]

[†]The Blackett Laboratory, Department of Physics, Imperial College London, London SW7 2AZ, United Kingdom

[§]Department of Electrical and Computer Engineering, University of California, San Diego, La Jolla, California 92093-0407, United States

Supporting Information

ABSTRACT: We present a far-field super-resolution imaging scheme based on coherent scattering under a composite photonic–plasmonic structured illumination. The super-resolved image retrieval method, which involves the combination of 13 different diffraction-limited images of the specimen, is first developed within a Fourier optics framework. A feasible implementation of this optical microscopy technique working at 465 nm is proposed and its point spread function is investigated using full electromagnetics calculations. The 4-fold super-resolution power of the scheme, able to resolve 60 nm feature sizes at the operating wavelength, is demonstrated against both Abbe's (imaging a single object) and Rayleigh's (imaging two closely spaced objects) criteria.

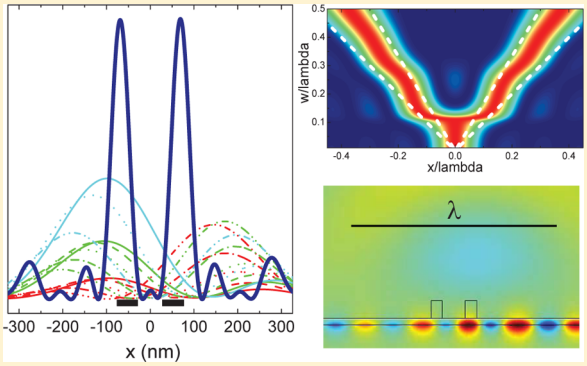

KEYWORDS: *optical super-resolution, far-field imaging, surface plasmons, coherent structured illumination*

The enormous advances in optical microscopy during the last decades have changed radically our understanding of the diffraction limit of light.[1,2] A wide range of strategies have been developed to overcome what was first thought as an inviolable constraint for optical resolution. All these schemes have made super-resolution[3] imaging possible, but this always comes at a price in terms of other microscope attributes such as speed, field of view, depth of focus, robustness, or versatility. Therefore, this set of techniques can be considered as a nanoscopic toolbox which offers a trade-off between resolution and other image characteristics beyond the diffraction limit.[4,5]

The exploitation of the negative permittivity of metals has proven to be a fruitful avenue to push optical resolution deep into the nanoscale. The use of metals to achieve super-resolution has led to the emergence of novel approaches, such as the superlens[6−8] or the hyperlens,[9−11] as well as the further development of previously established techniques, such as the near-field scanning optical microscope.[12,13] Only very recently, much research attention has been focused on the synergic combination[14] of surface plasmon nanophotonics[15] and far-field high-resolution fluorescence microscopy techniques.[16] These schemes, which include methods like stimulated emission depletion[17] or stochastic optical reconstruction,[18] have meant a conceptual and practical breakthrough in super-resolution imaging under incoherent illumination. During the last number of years, plasmonic devices designed to engineer the radiative properties of nanoemitters have been implemented in techniques such as photoactivation localization,[19] stimulated emission depletion,[20] or structured illumination[21] microscopies. This has allowed an unprecedented control over the spatial and temporal characteristics of the incoherent light sources exploited in all these far-field super-resolution methods.

Among the wide family of far-field fluorescent imaging techniques, structured illumination microscopy[22−24] (SIM) stands out for its fast and highly parallelizable character, which makes it specially suitable for in vivo biological applications.[25,26] However, the free-propagating nature of the structured illumination fields restricts its resolution power to a 2-fold improvement with respect to diffraction-limited microscopy (DLM). Several approaches have been investigated lately overcoming this constraint and realizing tunable standing-wave light patterns with features below half the operating wavelength. Apart from the aforementioned plasmonic platforms,[21,27] other proposals exploit high refractive index dielectrics,[28,29] spatial light modulators,[30,31] or nonlinear effects in the fluorescent emission pattern.[32,33] Importantly, SIM presents another very relevant feature. Although most SIM set-ups are based on incoherent light sources, structure illumination ideas can also be used to achieve subdiffraction resolution through coherent scattering from nonfluorescent specimens.[34−36] This fact provides the method with exceptional flexibility, as it can be applied in nonfluorescent environments inaccessible for most far-field microscopies.

In this work, we propose a coherent imaging scheme yielding 4-fold super-resolution on nonfluorescent objects illuminated

Received: September 16, 2014
Published: January 16, 2015

DOI: 10.1021/ph500342g
ACS Photonics 2015, 2, 341−348

by a photonic−plasmonic standing-wave pattern. This composite structured illumination microscopy (CSIM) approach exploits the spatial frequency mixing that takes place in the coherent scattering of the incident fields with the specimen. Through the linear combination of a set of diffraction-limited images taken for different configurations of the illumination, a 4-fold super-resolved image of the sample can be constructed. The image retrieval method minimizing the number of diffraction-limited images (and therefore optimizing the super-resolution imaging speed) is developed within the Fourier optics (FO) description.[37] Finally, its validity is demonstrated beyond the paraxial approximation through full electromagnetic (EM) calculations modeling a feasible implementation of the technique operating at 465 nm.

Our CSIM proposal is introduced in Figure 1. The square of the point spread function (PSF) and the coherent transfer function (CTF) for a DLM are rendered in gray in the right and central panels of Figure 1a. A schematic picture of the illumination is depicted in the top left panel, showing a plane wave impinging from the top and lacking of any spatial structure within the object plane (x-direction). Note that the diffraction-limited CTF, $C_{DLM}(m)$, is modeled through an abrupt low-pass filter ranging from $-m_0$ to m_0, where, for simplicity, we assume a numerical aperture (NA) equal to 1, and $m_0 = k_0/2\pi = 1/\lambda$ (see Supporting Information).

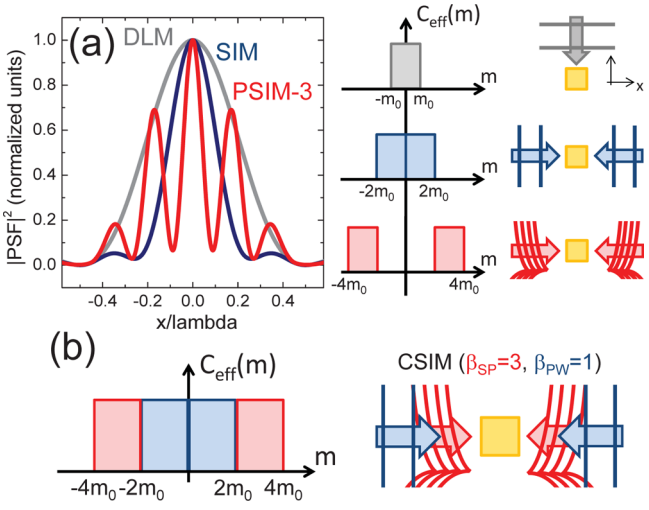

Figure 1. (a) Point spread function squared (left) and coherent transfer function (center) for a diffraction-limited microscope (gray) and a conventional SIM (blue). The square of the PSF and CTF for a PSIM with $\beta = 3$ are shown in red. The right panels sketch the illumination in each case. (b) Effective CTF and the illumination required for our 4-fold super-resolution CSIM proposal.

The PSF squared and CTF for a conventional SIM are shown in blue in Figure 1a. By using a photonic (free-propagating) standing-wave, which within the FO frame is described as $E(x) = \cos(k_0 x + \varphi/2)$, an effective transfer function twice wider than the DLM can be realized. Note that this resolution enhancement can also be achieved using two independent oblique illuminations instead of a sanding-wave pattern.[38] The SIM scheme requires the linear combination of 3 diffraction-limited images taken from the object for 3 different values of the parameter φ (which controls the position of the illumination nodes and antinodes within the object plane). See ref 34 for a detailed description of the coherent SIM methodology. Red color corresponds to the same imaging scheme but replacing the incident fields by a plasmonic standing-wave with a propagating constant $\beta = 3$ (defined as the ratio between the wave-vector component along x-direction and k_0). We term this case as PSIM-3, borrowing the notation introduced in previous literature.[21]

Figure 1a shows that, by using a plasmonic structured illumination, object features well below the diffraction limit are retained in the PSIM-3 image. The effective CTF, in this case, covers spatial frequencies up to $\pm 4m_0$, but also presents a gap for $|m| < 2m_0$. This means that the spatial information lying within this band is lost in the final image. Thus, the corresponding PSF presents a sharper central maximum but at the expense of significant side lobes that deform the image. Note that these resemble very much the artifacts associated with the apodization method,[39] whose near-field correction led to the emergence of scanning confocal microscopy.[40] Figure 1b illustrates our CSIM strategy aiming to overcome this obstacle in the far-field. It consists in using a coherent superposition of a photonic and a plasmonic standing-wave (see right panel) as the structured illumination. This way, it must be possible to construct images retaining both high ($2m_0 < |m| \leq 4m_0$) and low ($|m| < 2m_0$) spatial frequencies from the object (see the effective transfer function in the left panel) and obtain full 4-fold super-resolution.

The starting point for the construction of the CSIM image retrieval method is the comparison between two different microscopes. First, we consider an ideal, unphysical 4-fold super-resolution device that presents an inherent CTF like the one shown in Figure 1b. This transfer function can be expressed in terms of $C_{DLM}(m)$ as

$$C_{\times 4}(m) = C_{DLM}(m - 3m_0) + C_{DLM}(m - m_0) + C_{DLM}(m + m_0) + C_{DLM}(m + 3m_0) \quad (1)$$

The 4-fold super-resolved images obtained from this microscope under plane-wave illumination, $E(x) = E_0$, can be written within the FO framework as

$$I_{\times 4}(x) = 2(S_0(x) + T_1(x) + V_-(x) + V_+(x) + T_3(x)) \quad (2)$$

where each image component carries different spatial frequency information. $T_1(x)$ and $T_3(x)$ describe the EM intensity transmitted through $C_{DLM}(m \pm m_0)$ and $C_{DLM}(m \pm 3m_0)$, respectively. The V-terms reflect the coherent cross-talk between these two different spatial frequency windows. Finally, $S_0(x)$ takes into account the superposition of the EM fields transferred through $C_{DLM}(m - 3m_0)$ ($C_{DLM}(m - m_0)$) and $C_{DLM}(m + 3m_0)$ ($C_{DLM}(m + m_0)$). In the Supporting Information, a detailed derivation of eq 2 can be found, as well as the expressions for the various image components as a function of the various terms in eq 1.

The second imaging setup consists of a diffraction-limited microscope and the CSIM illumination described above. The incident electric field can be expressed as

$$E_{CSIM}(x) = \cos\left(k_0 x + \frac{\varphi_{PW}}{2}\right) + A_{SP} \cos\left(\beta_{SP} k_0 x + \frac{\varphi_{SP}}{2}\right) \quad (3)$$

where φ_{PW} and φ_{SP} are the phases that control the position of the nodes and antinodes of the photonic (PW) and plasmonic (SP) illumination components, and A_{SP} and β_{SP} are the relative amplitude and propagation constant of the SP standing-wave. It

DOI: 10.1021/ph500342g
ACS Photonics 2015, 2, 341−348

can be demonstrated (see Supporting Information) that the DLM images obtained from $E_{CSIM}(x)$ evaluated at $\beta_{SP} = 3$ have the form

$$I_{CSIM}(x) = 2(S_{01}(x) + A_{SP}^2 r_{SP}^2 S_{03}(x)) + 2(T_1(x)\cos(2k_0x - \varphi_{PW}) + U_1(x)\sin(2k_0x - \varphi_{PW})) + 2A_{SP}r_{SP}\left(V_-(x)\cos\left(2k_0x - \frac{\varphi_{SP} - \varphi_{PW}}{2}\right) + W_-(x)\sin\left(2k_0x - \frac{\varphi_{SP} - \varphi_{PW}}{2}\right)\right) + 2A_{SP}r_{SP}\left(V_+(x)\cos\left(4k_0x - \frac{\varphi_{SP} + \varphi_{PW}}{2}\right) + W_+(x)\sin\left(4k_0x - \frac{\varphi_{SP} + \varphi_{PW}}{2}\right)\right) + 2A_{SP}^2 r_{SP}^2(T_3(x)\cos(6k_0x - \varphi_{SP}) + U_3(x)\sin(6k_0x - \varphi_{SP})) \quad (4)$$

where r_{SP} is the reflection (or transmission, depending on the microscope configuration) coefficient for the specimen under the incident SP fields, normalized to the reflectivity (transmissivity) for the PW component of the illumination. This parameter is introduced to reflect that, in general, the optical response of the imaged object depend on the incident wavevector. Note that, by construction (see Supporting Information), $S_{01}(x) + S_{03}(x) = S_0(x)$, and therefore, all the super-resolved terms in eq 2 are also present in eq 4.

The CSIM image retrieval method detailed in the Supporting Information shows that 13 different $I_{CSIM}(x)$ are required to extract $I_{\times 4}(x)$. This number is given by the minimum set of coefficients required to build each of the terms in eq 2 through linear combinations of purely intensity (without any phase information) diffraction-limited images. This procedure require CSIM illuminations involving five different φ_{SP} and three different φ_{PW} (importantly, any SP and PW phases can be chosen). In order to avoid further, time-consuming, image postprocessing treatments, the relative amplitude of the incident SP standing-wave can be calibrated a priori (through the imaging of a reference sample with the SP and PW components of the illumination separately) so that $A_{SP}r_{SP} = 1$ in eq 4 (see Supporting Information). This is equivalent to set the same amplitude for the scattered waves originated from the SP and PW components of the illumination.

Figure 2a shows FO calculations for the CSIM imaging of a 1D object of width $a = 0.1\lambda$. Note that by operating on a specimen smaller than the resolution expected for our microscope, the square of the effective PSF for our CSIM approach can be directly obtained. In the background, the 13 DLM images used to build the super-resolved image are shown. These were obtained using the diffraction-limited PSF, $h_{DLM}(x) = F[C_{DLM}(m)]$ (where $F^{-1}[\cdot]$ denotes the Fourier transform). The colors indicate the choice of PW phases in eq 3: red (50°), green (100°) and cyan (150°). The line profiles label φ_{SP}: solid (30°), dashed (60°), dotted (90°), dotted-dashed (120°) and double-dotted-dashed (150°). Note that the two DLM images corresponding to (φ_{PW} = 150°, φ_{SP} = 30°) and (φ_{PW} = 150°, φ_{SP} = 150°) were not needed to construct the CSIM 4-fold super-resolved image rendered by the dark blue line in Figure 2a. As expected, this image exactly overlaps with $I_{\times 4}(x)$ calculated directly for an ideal microscope with a CTF given by

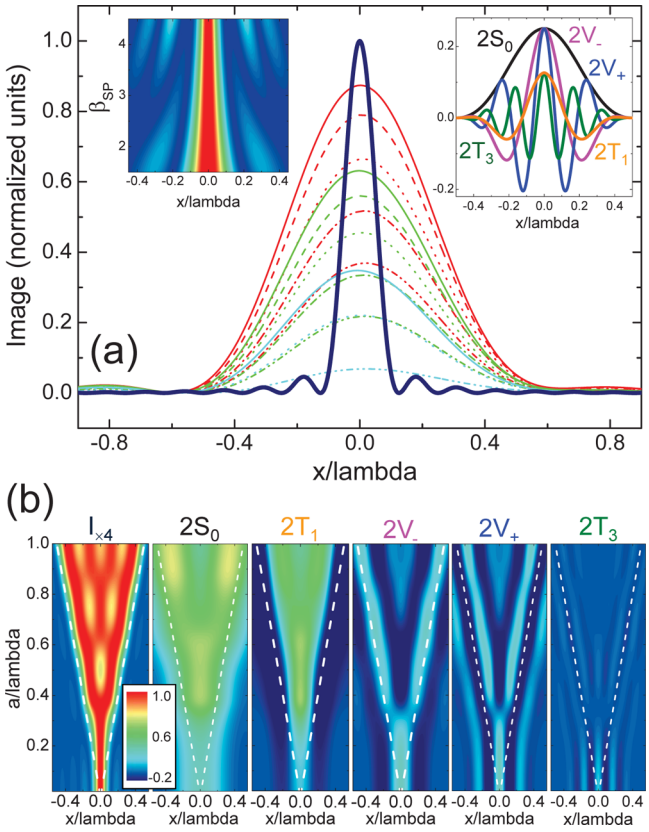

Figure 2. (a) Fourier optics CSIM image of a deeply subwavelength ($a = 0.1\lambda$) object (dark blue) obtained from the 13 diffraction-limited images rendered in the background: red, green, and cyan colors correspond to φ_{PW} = 50, 100, and 150°, respectively, and solid, dashed, dotted, dotted-dashed, and double-dotted-dashed lines to φ_{SP} = 30, 60, 90, 120, and 150°. The right inset plots the various components of the super-resolved image. The left inset shows the sensitivity of the CSIM effective PSF against variations in β_{SP}. The color scale ranges from 0 (dark blue) to 1 (red). (b) FO CSIM images (and the various image components) for 1D objects of width a ranging from 0.01λ to λ. The object edges are shown in white dashed lines.

eq 1. A direct comparison between Figure 2a and Figure 1 evidence the 4-fold (2-fold) sharpening of the effective PSF in our CSIM approach with respect to the DLM (SIM) schemes. In the left inset, the sensitivity of the CSIM super-resolved image ($a = 0.1\lambda$) against the SP propagation constant is shown. The contour plot reveals that for $\beta_{SP} > 3$, the super-resolved image develops side lobes in a similar way as the PSIM-3 image in Figure 1a. On the contrary, by decreasing this parameter, the CSIM $I_{\times 4}(x)$ broadens and approaches the SIM image in Figure 1a.

The right inset of Figure 2a plots the various terms in eq 2 for the super-resolved image in the main panel. Note that these components present positive and negative values, so that their superposition leads to a reshaped, non-negative, final image of the specimen. As we anticipated, each term carries distinct spatial information on the object. They exhibit different oscillation pitches along x-direction, given by the arguments of the trigonometric functions in eq 4 (note that $2T_1(x)$ and $2V_-(x)$ present the same oscillation pitch but different amplitude). In Figure 2b CSIM super-resolved images for 1D objects of width a ranging from 0.01λ to λ are shown (left panel). Note that the images sharpen with decreasing a down to $\lambda/8$, where they saturate evidencing that smaller objects are

DOI: 10.1021/ph500342g
ACS Photonics 2015, 2, 341−348

beyond the resolution power of the scheme. Figure 2b renders the super-resolved image components as a function of a/λ. These panels illustrate the spatial information behind each term in eq 2. Thus, $2S_0(x)$ and $2T_1(x)$ reflect the bulk of the object for $a \leq \lambda/2$, with edge corrections given by $2V_-(x)$ and $2V_+(x)$ and a negligible contribution from $2T_3(x)$. On the other hand, for $a < \lambda/4$, the amplitude of $2V_+(x)$ and $2T_3(x)$ are significantly larger and become comparable to the other components.

We have verified our imaging method within the FO frame. In order to demonstrate the super-resolution power of our proposal beyond the scalar, paraxial approximation inherent to this treatment, we present next a rigorous EM description of a feasible CSIM implementation. Importantly, we propose here a proof-of-principle realization of CSIM imaging, the development of an optimized setup is beyond the scope of this work. Our approach consists in generating full EM (diffraction-limited) images for different illumination configurations and combine them following the recipes introduced above, which are based on FO assumptions. Figure 3a shows a schematic

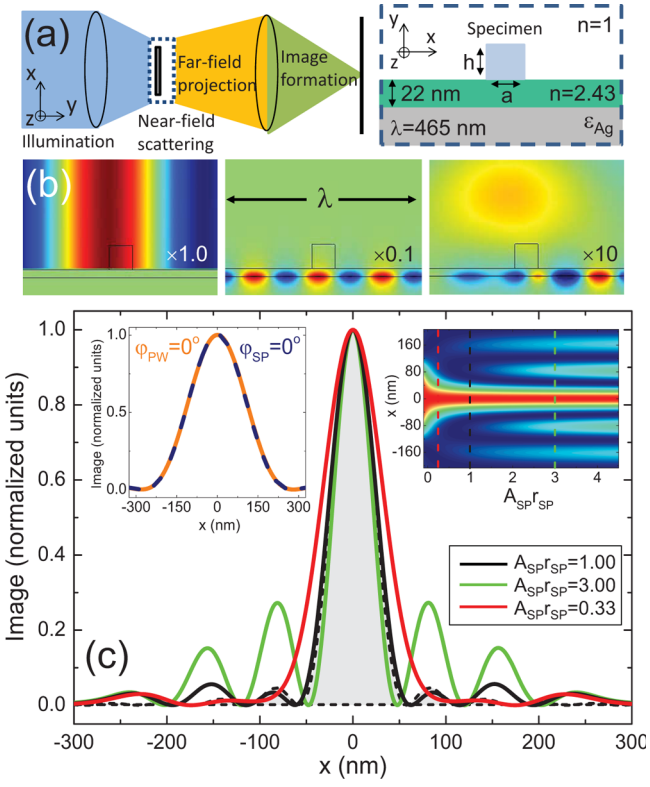

Figure 3. (a) Left: Schematics of the full EM modeling of a CSIM setup. Right: Near-field of the specimen. (b) Re$\{H_z\}$ for the PW (left) and SP (center) component of the illumination, and Im$\{H_z\}$ (right) for the total scattered fields ($\varphi_{PW} = 100°$, $\varphi_{SP} = 90°$). The dimensions and refractive index of the specimen are $a = h = 46$ nm and $n_S = 1.3$ ($\lambda = 465$ nm). The color scale ranges from red (positive) to blue (negative). Note the different amplitude factors. (c) EM CSIM image for the same object and different SP incident amplitudes. The black line is evaluated at $A_{SP}r_{SP} = 1$, and the corresponding FO prediction is rendered in shaded black dashed line. Red and green lines are EM images for $A_{SP}r_{SP} = 0.33$ and 3.0, respectively. The left inset shows the images obtained for both components of the illumination independently ($\varphi_{SP} = \varphi_{PW} = 0$) for $A_{SP}r_{SP} = 1$. The right inset shows the sensitivity the full EM CSIM image against variations in A_{SP}. The color scale renders the image intensity from 0 (blue) to 1 (red).

picture of our model for a realistic CSIM design. As our analysis has a fundamental purpose, we assume translational symmetry along the z-direction, which allows us to consider only transverse magnetic fields within the xy-plane. Four aspects of the imaging process need to be taken into account independently: the illumination, the coherent scattering in the near-field of the specimen, the far-field propagation of the scattered fields, and the image formation in a diffraction-limited, high NA microscope.[41]

We simplify the EM description of the composite photonic–plasmonic standing-wave to its injection in the near-field of the specimen. We omit a detailed treatment of its far-field realization and near-field coupling, which is beyond the scope of this work. Briefly, a CSIM platform would require the combination of a standard SIM configuration[24] and a setup similar to the ones recently implemented for highly tunable plasmonic focusing.[39,42] In these systems, plasmon standing wave patterns are produced through engineered coupling from an incident laser beam,[43,44] and the position of the illumination maxima (plasmon phase) is controlled through the angle of incidence of the incoming light.[21] Thus, the CSIM illumination would be obtained by splitting an initial laser beam into two components, controlling their relative phase and amplitude in the procedure. These two beams would then be used to generate the PW and SP standing waves whose coherent interference forms the final electromagnetic fields pattern. The left panel in Figure 3a depicts the near-field of the specimen as well as the metal-dielectric structure that we use as our CSIM platform (we assume that $n = 1$ for the background medium). The geometry is designed to support a surface plasmon polariton mode at $\lambda = 465$ nm (from now on, the operating wavelength) with a propagation constant $\beta_{SP} = 3.0 + 0.1i$. The refractive index for the 22 nm thick dielectric layer and the metal permittivity are taken from experimental data for GaN[45] and epitaxial silver,[46] respectively. Importantly, recent advances in the synthesis and fabrication of low-loss high refractive index dielectrics, such as GaP,[47,48] make these materials promising candidates for CSIM platforms presenting a much larger field of view.

Using Comsol Multiphysics, the coherent scattering of the CSIM incident fields with the specimen can be calculated numerically. The z-component of the magnetic field, H_z, for the composite photonic–plasmonic standing-wave illumination is injected analytically in each region of the system, and Maxwell Equations are solved for the scattered fields. Note that a similar configuration has been used recently for the modeling of dark-field spectroscopy experiments.[49] Figure 3b shows H_z snapshots for the PW (left) and SP (center) components of the illumination, as well as the total scattered fields (right) for an object with $a = h = 46$ nm ($\sim 0.1\lambda$) and refractive index $n_S = 1.3$. Note the numerical scale in each panel. The propagation of the scattered fields away from the sample is described using the Stratton-Chu theorem,[50] which provides a rigorous near-to-far-field projection of the electric field. Finally, we treat the image formation through the diffraction limited microscope in our CSIM setup using the Debye-Wolf integral formalism,[51] which is a suitable approach for the modeling of optical focusing through a high NA lens.[41]

The black line in Figure 3c plots the full EM 4-fold CSIM image obtained for the square object shown in panel (b). $I_{\times 4}(x)$ was built from the EM images obtained through the procedure discussed above for illuminations with the same PW and SP phases as the ones considered in Figure 2a. For comparison, the

DOI: 10.1021/ph500342g
ACS Photonics 2015, 2, 341–348

FO prediction is also shown in black dashed shaded line. The agreement is excellent, and proves the validity of our imaging scheme and its 4-fold super-resolution power. The left inset shows diffraction-limited EM images obtained from the specimen under the PW and SP components of the illumination separately, evaluated at $\varphi_{PW} = 0$ and $\varphi_{SP} = 0°$, respectively. The fact that both images overlap indicates that our illumination satisfies the condition $A_{SP}r_{SP} = 1$.

The contour plot in the right panel of Figure 3c investigates the robustness of the super-resolved image against variations in the SP amplitude of the illumination. For smaller (larger) plasmonic amplitudes, $A_{SP}r_{SP} < 1$ ($A_{SP}r_{SP} > 1$), and the image broadens (develops side lobes) in a similar way as we observed in Figure 2a by decreasing (increasing) β_{SP}. This effect is clearly observed in the red and green lines in the main panel, which correspond to $I_{\times 4}(x)$ calculated for $A_{SP}r_{SP} = 0.33$ and 3.0, respectively. Note that the dependence of the CSIM images on the relative scattered amplitude can be also interpreted in terms of the absorption losses experienced by the SP component of the illumination, which presents a propagation decay length $L_{SP} = \lambda/(2\pi \mathrm{Im}\{\beta_{SP}\}) = 1.6\lambda$ (defined in terms of field amplitude). Thus, shifting the position of the specimen by 820 nm would be equivalent to a factor 3 reduction in $A_{SP}r_{SP}$. This effectively constrains the microscope field of view to a few microns.

Our EM model for CSIM imaging does not only allow us to verify the scheme, but also to study the sensitivity of the implementation that we propose against configuration parameters that cannot be taken into account in a simple FO treatment. Figure 4a plots CSIM super-resolved images (λ = 465 nm) for a single, square object of side 46 nm, and different refractive indices ranging from 1.05 to 1.5. In all cases, the illumination amplitudes were set to yield $A_{SP}r_{SP} = 1$ following the same procedure as in Figure 2c. The images show that the CSIM imaging scheme can operate at low refractive index contrasts, as the effective PSF varies only very slightly from n_S = 1.5 to 1.1. For $n_S = 1.05$, $I_{\times 4}(x)$ is distorted and develops significant side lobes. These are originated from substrate effects in the scattering of the incident fields and the specimen. In the FO description, these are not taken into account, and hence, they are neglected in the CSIM image retrieval method. The occurrence of multiple scattering and significant field enhancement at the metal-dielectric interface of the CSIM substrate can be observed in the left panel of Figure 2b.

The left inset of Figure 4a plots the SP amplitude of the illumination used to generate the images in the main panel versus the refractive index of the specimen. For reference, the data are normalized to the case $n_S = 1.3$. The variation of the SP amplitude is introduced to account for the change in the optical response of the object and satisfy the relation $A_{SP}r_{SP} = 1$ for all n_S. The panel indicates that a refractive index change of 0.1 requires a factor ~3 change in A_{SP}. Failing to introduce this amplitude correction leads to deviations from $I_{\times 4}(x)$ similar to the ones presented in Figure 3c.

The right inset in Figure 4a analyzes the dependence of the super-resolved CSIM images on another parameter characterizing the illumination, the standing-wave phases. Three different degrees of phase noise (indicated by a percentage of the nominal value) have been introduced in the EM fields modeling the CSIM illuminations, keeping the nominal phase values in the image retrieval recipes. Our results ($n_S = 1.3$, $a = h$ = 46 nm) indicate that the super-resolved image is completely blurred for noise levels of 10%, and develops side lobe oscillations of relative height 0.4 and 0.2 for 1% and 0.1%,

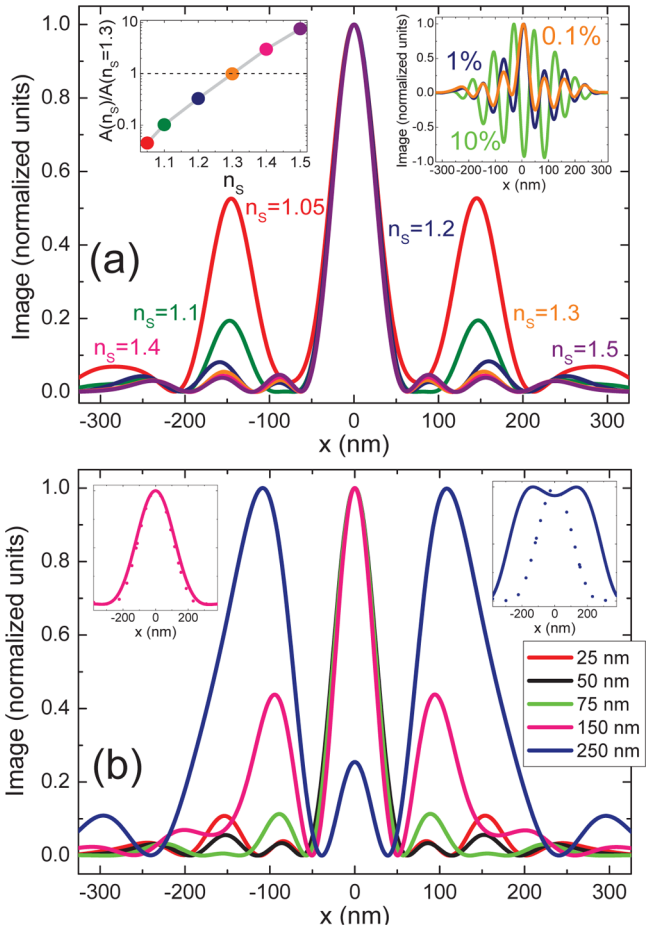

Figure 4. (a) Full EM CSIM image for a single specimen with $a = h$ = 46 nm and different refractive indices. The incident SP amplitude is calibrated to fulfill $A_{SP}r_{SP} = 1$ in each case. The left inset plots the calibrated SP amplitudes as a function of n_S. The right inset shows the CSIM PSF sensitivity to noise effects (expressed in %) in φ_{PW} and φ_{SP} (n_S = 1.3). (b) Super-resolved images for different gap distances between the object ($a = h$ = 46 nm, n_S = 1.3) and the CSIM substrate. The right and left insets plot the diffraction-limited images for the same object illuminated only with the SP ($\varphi_{SP} = 0°$) and PW (φ_{PW} = 0°) fields. Dotted and solid lines correspond to gap distances of 25 and 250 nm, respectively.

respectively. The sensitivity of our CSIM method to phase noise is similar to conventional SIM, where more robust-to-noise super-resolved images can be built by modifying the reconstruction procedure so that a larger amount of DLM images are used. This comes at the expense of lower operation speed.[52,53]

Next, we further investigate the impact of multiple scattering and substrate effects on our imaging scheme. Figure 4b renders CSIM images for various gap distances between the object in panel (a) and the metal-dielectric substrate. By varying this separation, the phase difference between the fields directly scattered by the specimen and those reflected from the metal-dielectric platform is modified (note that the latter are neglected in our CSIM image retrieval method). Thus, we use the gap distance to control the superposition between these two scattered field components and analyze the impact of substrate effects. The CSIM images in Figure 4b indicate that these only introduce minor distortions (in the form of side lobes) for separations up to 100 nm. However, for larger distances (250 nm), the phase accumulated in this multiple

DOI: 10.1021/ph500342g
ACS Photonics 2015, 2, 341−348

scattering gives rise to a complete distortion of $I_{\times 4}(x)$. This can be understood as a consequence of the fact that the scatterer is no longer optically thin, as it is assumed in our CSIM methodology (see Supporting Information). The left inset shows the DLM images obtained for 25 nm (dotted line) and 250 nm (solid line) separations under the SP component of the illumination only ($\varphi_{SP} = 0$). The right inset renders the same but for the PW fields ($\varphi_{PW} = 0$). Whereas the SP and PW images overlap for the 25 nm gap, substrate effects produce a great distortion in the image under PW illumination for a 250 nm distance. According to Figure 4b, we can set the depth of focus for our CSIM scheme below 120 nm ($\sim\lambda/4$).

Up to here, we have investigated the performance of our implementation of the CSIM scheme through the imaging of single, isolated objects. This way, and using Abbe's criterion,[1] we have demonstrated the $\lambda/8$ resolution power of the technique. However, many other criteria to assess optical resolution can be found in the literature. Among them, the so-called Rayleigh criterion,[54] which sets the minimum resolvable distance through the imaging of two closely spaced objects, is probably the most accepted. In the following, we present an analysis of CSIM resolution power in the spirit of the Rayleigh criterion. Specifically, we consider two $n_S = 1.3$, $h = 46$ nm objects of width $w/2$, separated by a gap of size w, and investigate the sample image for w ranging from 0 to 370 nm (0.8λ). Figure 5a–d display FO optics calculations describing the imaging of the system (the object edges are plotted in white dashed lines) under four different microscopes. Panels (a) and (b) show DLM and SIM images, which resolve the two objects down to $w = \lambda/2$ and $w = \lambda/4$, respectively. For smaller w, the two intensity maxima merge and the images present a single peak. Panel (c) evaluates the performance of the PSIM-3 microscope in Figure 1 and reveals the significant image distortions caused by the side lobes in its effective PSF. Note that panels (b) and (c) were generated through the combination of three DLM images.[34] Finally, panel (d) shows the CSIM images built using 13 diffraction-limited images of the specimen. In this panel, the two objects are apparent down to $\lambda/8$, in agreement with the 4-fold resolution power that the Abbe's criterion yields for the scheme.

Figure 5e shows the comparison between FO (shaded lines) and full EM (solid lines) CSIM images for different w, indicated in nanometers and in λ-units in each panel ($\lambda = 465$ nm). The bottom panel corresponds to a single, $a = 46$ nm, specimen taken as the reference to set the SP relative amplitude in the CSIM illuminations used for all the samples. In all cases, FO and EM predictions are in remarkable agreement, given that not only the object-substrate but also object–object multiple scattering effects that emerge in the EM calculations are not taken into account in the CSIM image retrieval method. Note that the two object can be clearly distinguished for $w = 0.15\lambda = 70$ nm, whereas they seem to merge for $w = 0.1\lambda = 0.46$ nm. Using a slight modification of the Rayleigh criterion,[55] we can conclude that the sample for $w = 0.13\lambda = 60$ nm is fully resolved, as the image intensity drops to half its maximum at the gap between the two objects.

Figure 5f,g render the EM $I_{\times 4}(x)$ for $w = 70$ and 60 nm, respectively, together with the DLM images used for their generation (shown in the background). The φ_{PW} and φ_{SP} values in the CSIM illuminations are the same (and follow the same color and profile codes) as in Figure 2a. Figure 5h plots the super-resolved CSIM image for an asymmetric configuration consisting of two objects of widths 30 nm (left) and 35 nm

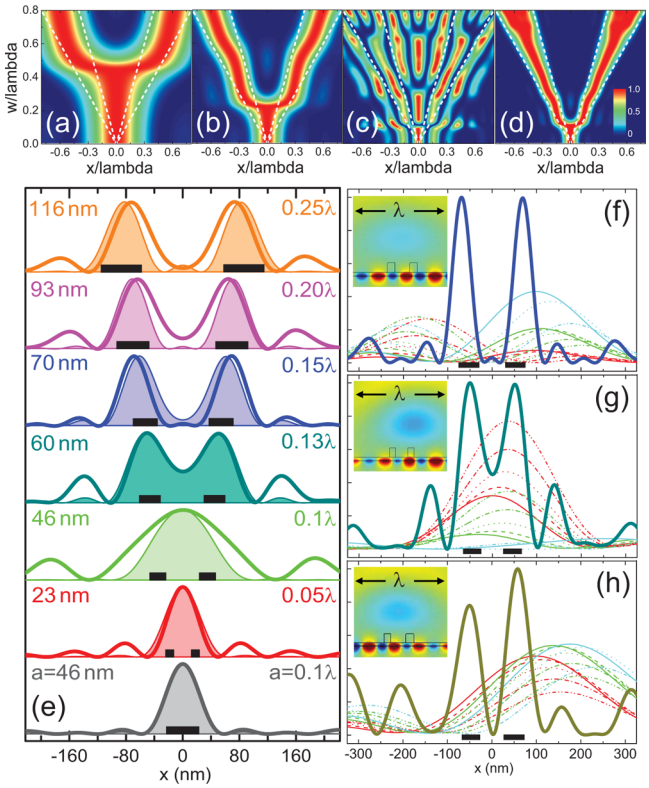

Figure 5. FO images for two objects of width $w/2$ separated by a gap of size w as a function of w/λ (the specimen edges are plotted in white dashed lines). The different panels correspond to the images obtained for DLM (a), conventional SIM (b), PSIM with $\beta_{SP} = 3$ (c), and CSIM (d). Solid (shaded) lines in panel (e) plot EM (FO) CSIM images for various w. The operating wavelength is set to 465 nm, and $n_S = 1.3$. Panels (f) and (g) plot the EM CSIM images for $w = 70$ and 60 nm, respectively. Panel (h) renders the asymmetric image obtained from two objects of widths 30 nm (left) and 35 nm (right) separated by 65 nm. The diffraction-limited images in these three panels are also shown, labeled as in Figure 2a. The insets render the scattered $\mathrm{Im}\{H_z\}$ for the values of φ_{PW} and φ_{SP} yielding the most intense image in each case.

(right), separated by a 65 nm gap (the corresponding DLM images are shown in the background). Note the drastic differences among the background images in these three panels. The insets display snapshots of the near-field scattered H_z for the incident illumination that yields the most intense image in each case. The high sensitivity of the diffraction-limited images to the sample geometry (note that there is only a 0.02λ difference in w between panels (f) and (g)) is the origin for the high resolution power of our CSIM proposal. Importantly, this sensitivity also explains the high impact that any deviation from the nominal characteristics of the illumination has on the final super-resolved CSIM image.

In all our calculations, we have assumed translational invariance along y-direction in our CSIM setup, which makes the images depend only on the x-coordinate. Importantly, the extension of our proposal to full 2D imaging does not require modifying our CSIM methodology. On the contrary, 4-fold super-resolved images from 3D specimens can be obtained by simply rotating the illumination plane. This way, the total number of diffraction-limited images required to achieve 2D 4-fold super-resolution is given by 13 times the number of illumination planes. Note that this is the mode of operation of most SIM schemes,[25,27,33] where the final image is constructed

DOI: 10.1021/ph500342g
ACS Photonics 2015, 2, 341–348

by adding the super-resolved SIM images collected in 3−5 azimuthal steps.

In conclusion, we have presented a theoretical proposal to achieve far-field 4-fold optical super-resolution on non-fluorescent samples. The scheme uses coherent scattering from a tunable composite photonic−plasmonic structured illumination. A super-resolved image retrieval method has been developed within the Fourier optics frame, requiring the linear combination of 13 diffraction-limited images to resolve spatial features down to $\lambda/8$. The approach has been verified through full electromagnetic simulations modeling its experimental implementation, which resolves object features down to 60 nm for a 465 nm operating wavelength. The sensitivity of this proof-of-concept setup against illumination parameters and specimen characteristics has been thoroughly analyzed. We have shown that it presents limitations in microscope attributes such as the field of view or phase-noise sensitivity, which are expected to be overcome in an optimized design. Finally, the resolution power of the imaging technique has been also proven through the systematic imaging of closely spaced objects. We believe that our fundamental findings offer novel possibilities in the scientific quest against the diffraction limit of classical optics, broadening the current microscopic imaging toolbox, and opening a promising technological pathway to push nonfluorescent far-field optical resolution deep into the nanoscale.

■ ASSOCIATED CONTENT

Supporting Information

Detailed Fourier optics description of our composite photonic−plasmonic structured illumination imaging scheme is presented. Section I provides a brief introduction to the fundamentals of coherent imaging theory. In Section II, our approach is motivated through the comparison with an intrinsic four-fold super-resolution device. In Section III, the image retrieval method behind our proposal is developed. Finally, in Section IV, the calibration of the relative amplitude between the photonic and plasmonic components of the illumination is discussed. This material is available free of charge via the Internet at http://pubs.acs.org.

■ AUTHOR INFORMATION

Corresponding Author

*E-mail: a.fernandez-dominguez@uam.es.

Present Address

‡Departamento de Física Teórica de la Materia Condensada and Condensed Matter Physics Center (IFIMAC), Universidad Autónoma de Madrid, E-28049 Madrid, Spain.

Notes

The authors declare no competing financial interest.

■ ACKNOWLEDGMENTS

This work was funded by the Gordon and Betty Moore Foundation.

■ REFERENCES

(1) Abbe, E. Beiträge zur theorie des mikroskops und der mikroskopischen wahrnehmung. *Arch. Mikr. Anat.* **1873**, *9*, 413−418.

(2) Stephenson, J. W. Observations on professor Abbe's experiments illustrating his theory of microscopic vision. *Am. Mon. Microsc. J.* **1877**, *17*, 82−88.

(3) Lukosz, W. Optical systems with resolving powers exceeding the classical limit. *J. Opt. Soc. Am.* **1966**, *56*, 1463−1472.

(4) Huang, B.; Babcock, H.; Zhuang, X. Breaking the diffraction barrier: super-resolution imaging of cells. *Cell* **2010**, *143*, 1047−1058.

(5) Hao, X.; Kuang, C.; Gu, Z.; Wang, Y.; Li, S.; Ku, Y.; Li, Y.; Ge, J.; Liu, X. From microscopy to nanoscopy via visible light. *Light: Sci. Appl.* **2013**, *2*, e108.

(6) Pendry, J. B. Negative refraction makes a perfect lens. *Phys. Rev. Lett.* **2000**, *85*, 3966−3969.

(7) Fang, N.; Lee, H.; Sun, C.; Zhang, X. Sub-diffraction-limited optical imaging with a silver superlens. *Science* **2005**, *308*, 534−537.

(8) Liu, Z.; Durant, S.; Lee, H.; Pikus, Y.; Fang, N.; Xiong, Y.; Sun, C.; Zhang, X. Far-field optical superlens. *Nano Lett.* **2007**, *2*, 403−408.

(9) Salandrino, A.; Engheta, N. Far-field subdiffraction optical microscopy using metamaterial crystals: Theory and simulations. *Phys. Rev. B* **2006**, *74*, 075103.

(10) Jacob, Z.; Alekseyev, L. V.; Narimanov, E. E. Optical hyperlens: Far-field imaging beyond the diffraction limit. *Opt. Express* **2006**, *14*, 8247−8256.

(11) Liu, Z.; Lee, H.; Xiong, Y.; Sun, C.; Zhang, X. Far-field optical hyperlens magnifying sub-diffraction-limited objects. *Science* **2007**, *315*, 1686.

(12) Inouye, Y.; Kawata, S. Near-field scanning optical microscope with a metallic probe tip. *Opt. Lett.* **1994**, *19*, 159−161.

(13) Sánchez, E. J.; Novotny, L.; Xie, X. S. Near-field uorescence microscopy based on twi-photon excitation with metal tips. *Phys. Rev. Lett.* **1999**, *82*, 4014−4017.

(14) Balzarotti, F.; Stefani, F. D. Plasmonics meets far-field optical nanoscopy. *ACS Nano* **2012**, *6*, 4580−4584.

(15) Maier, S. A. *Plasmonics: Fundamentals and Applications*; Springer: New York, 2007.

(16) Galbraith, C. G.; Galbraith, J. A. Super-resolution microscopy at a glance. *J. Cell. Sci.* **2011**, *124*, 1607−1611.

(17) Hell, S. W.; Wichmann, J. Breaking the diffraction resolution limit by stimulated emission: Stimulated-emission-depletion uorescence microscopy. *Opt. Lett.* **1994**, *19*, 780−782.

(18) Rust, M.; Bates, M.; Zhuang, X. Sub-diffraction-limit imaging by stochastic optical reconstruction microscopy (STORM). *Nat. Methods* **2006**, *3*, 793−796.

(19) Wu, D.; Liu, Z.; Sun, C.; Zhang, X. Imaging by random adsorbed molecule probes. *Nano Lett.* **2008**, *8*, 1159−1162.

(20) Sivan, Y.; Sonnefraud, Y.; Kéna-Cohen, S.; Pendry, J. B.; Maier, S. A. Nanoparticle-assisted stimulated-emission-depletion nanoscopy. *ACS Nano* **2012**, *6*, 5291−5296.

(21) Wei, F.; Liu, Z. Plasmonic Structured Illumination Microscopy. *Nano Lett.* **2010**, *10*, 2531−2536.

(22) Heintzmann, R.; Cremer, C. Laterally modulated excitation microscopy: improvement of resolution by using a diffraction grating. *Proc. SPIE* **1998**, *3568*, 185−195.

(23) Gustafssonn, M. G. L. Surpassing the lateral resolution limit by a factor of two using structured illumination microscopy. *J. Microsc.* **2000**, *198*, 82−87.

(24) Frohn, J. T.; Knapp, H. F.; Stemmer, A. True optical resolution beyond the Rayleigh limit achieved by standing wave illumination. *Proc. Natl. Acad. Sci. U.S.A.* **2000**, *97*, 7232−7236.

(25) Schermelleh, L.; Carlton, P. M.; Haase, S.; Shao, L.; Winoto, L.; Kner, P.; Burke, B.; C, C. M.; Agard, D. A.; Gustafsson, M. G. L.; Leonhardt, H.; Sedat, J. W. Subdiffraction multicolor imaging of the nuclear periphery with 3D structured illumination microscopy. *Science* **2008**, *320*, 1332−1336.

(26) Langhorst, M. F.; Schaffer, J.; Goetze, B. Structure brings clarity: structured illumination microscopy in cell biology. *Biotechnol. J.* **2009**, *4*, 858−865.

(27) Ponsetto, J. L.; Wei, F.; Liu, Z. Localized plasmon assisted structured illumination microscopy for wide-field high-speed dispersion-independent super resolution imaging. *Nanoscale* **2014**, *17*, 5807−5812.

(28) Sentenac, A.; Chaumet, P. C.; Belkebir, K. Beyond the rayleigh criterion: grating assisted far-field optical diffraction tomography. *Phys. Rev. Lett.* **2006**, *97*, 243901.

DOI: 10.1021/ph500342g
ACS Photonics 2015, 2, 341−348

(29) Girard, J.; Scherrer, G.; Cattoni, A.; Le Moal, E.; Talneau, A.; Cluzel, B.; de Fornel, F.; Sentenac, A. Far-field optical control of a movable subdiffraction light grid. *Phys. Lett.* **2012**, *109*, 187404.
(30) Fiolka, R.; Beck, M.; Stemmer, A. Structured illumination in total internal reection uorescence microscopy using a spatial light modulator. *Opt. Lett.* **2008**, *33*, 1629−1631.
(31) Gjonaj, B.; Aulbach, J.; Johnson, P. M.; Mosk, A. P.; Kuipers, L.; Lagendijk, A. Optical control of plasmonic bloch modes on periodic nanostructures. *Nano Lett.* **2012**, *12*, 546−550.
(32) Gustafsson, M. G. L. Nonlinear structured-illumination microscopy: Wide-field uorescence imaging with theoretically unlimited resolution. *Proc. Natl. Acad. Sci. U.S.A.* **2005**, *102*, 13081−13086.
(33) Rego, E. H.; Shao, L.; Macklin, J. J.; Winoto, L.; Johansson, G. A.; Kamps-Hughes, N.; Davidson, M. W.; Gustafsson, M. G. L. Nonlinear structured-illumination microscopy with a photoswitchable protein reveals cellular structures at 50-nm resolution. *Proc. Natl. Acad. Sci. U.S.A.* **2012**, *109*, E135−E143.
(34) Littleton, B.; Lai, K.; Longstaff, V.; Dannis abd Sarafis; Munroe, P.; Heckenberg, N.; Rubinsztein-Dunlop, H. Coherent super-resolution microscopy via laterally structured illumination. *Micron* **2007**, *38*, 150−157.
(35) Chowdhury, S.; Dhalla, A.-H.; Izatt, J. Structured oblique illumination microscopy for enhanced resolution imaging of non-uorescent, coherently scattering samples. *Biomed. Opt. Express* **2012**, *3*, 1841−1854.
(36) Dan, D.; Lei, M.; Yao, B.; Wang, W.; Winterhalder, M.; Zumbusch, A.; Qi, Y.; Xia, L.; Yan, S.; Yang, Y.; Gao, P.; Ye, T.; Zhao, W. DMD-based LED-illumination superresolution and optical sectioning microscopy. *Sci. Rep.* **2013**, *3*, 1116.
(37) Goodman, J. W. *Introduction to Fourier Optics*; McGraw-Hill: Columbus, OH, 1996.
(38) Wicker, K.; Heintzmann, R. Resolving a misconception about structured illumination. *Nat. Photonics* **2014**, *8*, 342−344.
(39) Wang, H.; Sheppard, J. R.; Ravi, K.; Jo, S. T.; Vienne, G. Fighting against diffraction: apodization and near field diffraction structures. *Laser Photonics Rev.* **2012**, *6*, 354−392.
(40) Wilson, T. Resolution and optical sectioning in the confocal microscope. *J. Microsc.* **2011**, *244*, 113−121.
(41) Török, P.; Munro, P. R. T.; Kriezis, E. E. High numerical aperture vectorial imaging in coherent optical microscopes. *Opt. Express* **2008**, *16*, 507−523.
(42) Liu, Z.; Steele, J. M.; Srituravanich, W.; Pikus, Y.; Sun, C.; Zhang, X. Focusing surface plasmons with a plasmonic lens. *Nano Lett.* **2005**, *5*, 1726−1729.
(43) López-Tejeira, L.; Rodrigo, S. G.; Martín-Moreno, L.; García-Vidal, F. J.; Devaux, E.; Ebbesen, T. W.; Kreenn, J. R.; Radko, I. P.; Bozhevolnyi, S. I.; González, M. U.; Weeber, J. C.; Dereux, A. Effcient unidirectional nanoslit couplers for surface plasmons. *Nat. Phys.* **2007**, *3*, 324−328.
(44) Huang, X.; Brongersma, M. L. Compact aperiodic metallic groove arrays for unidirectional launching of surface plasmons. *Nano Lett.* **2013**, *13*, 5420−5424.
(45) Yu, G.; Wang, G.; Ishikawa, H.; Umeno, M.; Soga, T.; Egawa, T.; Watanabe, J.; Jimbo, T. Optical properties of wurtzite structure GaN on sapphire around fundamental absorption edge (0.78−4.77 eV) by spectroscopic ellipsometry and the optical transmission method. *Appl. Phys. Lett.* **1997**, *70*, 3209−3211.
(46) Wu, Y.; Zhang, C.; Zhao, Y.; Kim, J.; Zhang, M.; Liu, X. X.; Pribi, G. K.; Alu, A.; Shih, C. K.; Li, X. Intrinsic optical properties and enhanced plasmonic response of epitaxial silver. *Adv. Mater.* **2014**, *26*, 6106−6110.
(47) Rivoire, R.; Faraon, A.; Vuckovic, J. Gallium phosphide photonic crystal nanocavities in the visible. *Appl. Phys. Lett.* **2008**, *93*, 063103.
(48) Albella, P.; Alcaraz de la Osa, R.; Moreno, F.; Maier, S. A. Electric and magnetic field enhancement with ultralow heat radiation dielectric nanoantennas: considerations for surface- enhanced spectroscopies. *ACS Photonics* **2014**, *1*, 524−529.
(49) Lei, D. Y.; Fernández-Domínguez, A. I.; Sonnefraud, Y.; Knnatassen, A.; Haglund, R. F.; Pendry, J. B.; Maier, S. A. Revealing plasmonic gap modes in particleon- film systems using dark-field spectroscopy. *ACS Nano* **2012**, *6*, 1380−1386.
(50) Stratton, J. A.; Chu, L. J. Diffraction theory of electromagnetic waves. *Phys. Rev.* **1936**, *56*, 99−107.
(51) Richards, B.; Wolf, E. Electromagnetic diffraction in optical systems. II. Structure of the image field in an aplanatic system. *Proc. R. Soc. London* **1959**, *253*, 358−379.
(52) Mudry, E.; Belkebir, K.; Girard, J.; Savatier, J.; Le Moal, E.; Nicoletti, C.; Allain, M.; Sentenac, A. Structured illumination microscopy using unknown speckle patterns. *Nat. Photonics* **2012**, *6*, 312−315.
(53) Ayuk, R.; Giovannini, H.; Jost, A.; Mudry, E.; Girard, J.; Mangeat, T.; Sandeau, N.; Heintzmann, R.; Wicker, K.; Belkebir, K.; Sentenac, A. Structured illumination uorescence microscopy with distorted excitations using a filtered blind-SIM algorithm. *Opt. Lett.* **2013**, *38*, 4723−4726.
(54) Rayleigh, L. On the manufacture and theory of diffraction-gratings. *Philos. Mag.* **1874**, *47*, 81−93.
(55) Houston, W. V. A compound interferometer for fine structure work. *Phys. Rev.* **1927**, *29*, 0478−0484.

DOI: 10.1021/ph500342g
ACS Photonics 2015, 2, 341−348